Polymer 51 (2010) 1830–1836

Contents lists available at ScienceDirect

Polymer

journal homepage: www.elsevier.com/locate/polymer

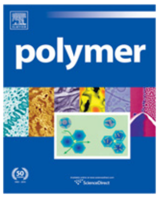

Poly(ethylene terephthalate) nanosheets prepared by CO_2-laser supersonic multi-drawing

Akihiro Suzuki*, Kyohei Arino

Interdisciplinary Graduate School of Medicine and Engineering, University of Yamanashi, Takeda-4, Kofu 400-8511, Japan

ARTICLE INFO

Article history:
Received 3 December 2009
Accepted 15 February 2010
Available online 19 February 2010

Keywords:
PET
Nanofiber
Nanosheet

ABSTRACT

Poly(ethylene terephthalate) (PET) nanosheets were fabricated by winding nanofibers onto a spool. The nanofibers were prepared by irradiating PET fibers with radiation from a carbon dioxide laser while drawing them at supersonic velocities. A supersonic jet was generated by blowing air into a vacuum chamber through the fiber injection orifice. A new vacuum chamber was developed to produce nanosheets; it has seven fiber injection orifices and a spool to collect the nanofibers. A rectangular nanosheet that was 17 cm wide, 18 cm long, and 30 μm thick was obtained by collecting nanofibers for 10 min. The nanosheet is composed of nanofibers with an average fiber diameter of 350 nm. This technique is a novel method for producing nanosheets.

1. Introduction

Nanofibers have been produced by electrospinning [1–9], melt electrospinning [10–12], sea–island-type conjugated melt spinning, single-orifice melt blowing [13], and jet blowing [14]. Electrospinning has been the leading method for preparing nanofibers.

We proposed a new approach for producing nanofibers [15]. It involves irradiating a fiber with radiation from a carbon dioxide (CO_2) laser while drawing the fiber at a supersonic velocity. A supersonic jet is generated by blowing air into a vacuum chamber through the orifice used to inject the fiber into the vacuum chamber. The adiabatic expansion of air across the orifice cools the jet. The fiber is instantly melted by the high-power laser beam that irradiates the cold supersonic jet. It is then tremendously deformed by the shear force generated by the supersonic flow, and ultra-drawn to a draw ratio of the order of 10^5. We named this preparation method *CO_2-laser supersonic drawing (CLSD)*. Supersonic drawing has already been applied to poly(L-lactic acid) [15], poly(ethylene terephthalate) (PET) [16], and poly(ethylene-2,6-naphthalate) [17], and fibers with average diameters of 132, 193, and 259 nm were respectively obtained. Nanofibers obtained by CLSD can be made indefinitely long because a fiber is supplied at a constant speed and it is continuously irradiated by a laser beam. CLSD can be used to easily prepare various nanofibers since it just employs CO_2-laser irradiation and does not require any additional processes or any solvents. CLSD prevents scattering of the nanofiber in air because it is performed in a vacuum chamber. It also offers superior environmental safety compared with electrospinning and melt blowing performed in open systems because it is conducted in a closed system.

Although CLSD can produce nanofibers with uniform fiber diameters, sheets produced from these nanofibers have low shape and thickness uniformities. We developed a modified CLSD technique, which we term *CO_2-laser supersonic multi-drawing (CLSMD)*, to form large nanosheets with high thickness uniformity. It employs a vacuum chamber with several fiber injection orifices and a winding spool to collect the nanofiber.

In this paper, we present preparation of PET nanosheets by CLSMD and analyze the properties of the PET nanosheets.

2. Experimental

The PET fibers used in the present study were prepared from commercial-grade PET pellets using a laboratory melt spinning machine. The as-spun PET fibers had an average diameter of 136 μm and were almost completely amorphous and isotropic (see Fig. 1).

The morphologies of the produced nanosheets were investigated by scanning electron microscopy (SEM) (JSM-6060LV, JEOL Ltd.) using an accelerating voltage of 10 kV. Prior to SEM observation, the samples were coated with gold using a sputter coater. The average diameter and the diameter distribution of the nanofibers were measured using an image analyzer. The average fiber diameter was determined by averaging the diameters measured at 100 different locations in a nanosheet.

Differential scanning calorimetry (DSC) measurements were conducted using a calorimeter (Therm Plus 2 DSC 8230C, Rigaku

---

* Corresponding author. Tel./fax: +81 55 220 8556.
E-mail address: a-suzuki@yamanashi.ac.jp (A. Suzuki).

0032-3861/$ – see front matter © 2010 Elsevier Ltd. All rights reserved.
doi:10.1016/j.polymer.2010.02.026

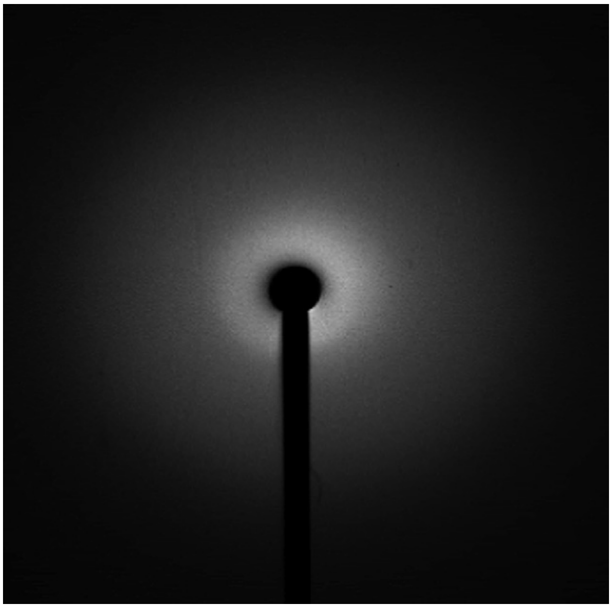

Fig. 1. Wide-angle x-ray diffraction pattern of original PET fiber.

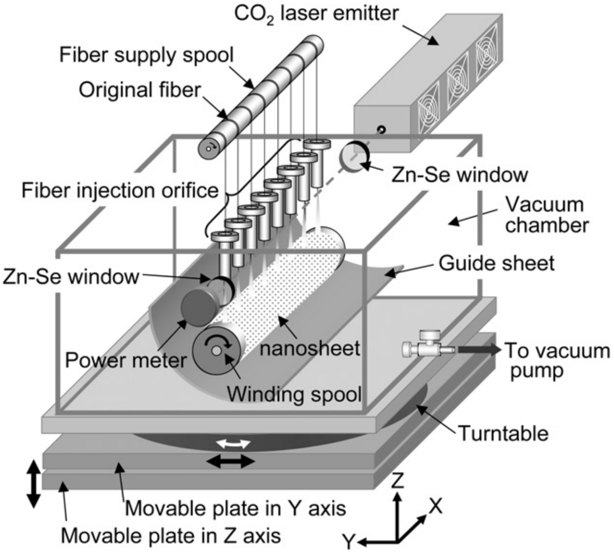

Fig. 2. Schematic diagram of apparatus used for CLSMD.

Co.). DSC scans were performed within the temperature range 25–280 °C at a heating rate of 10 °C min^{-1}. All DSC experiments were performed under a nitrogen purge. The DSC instrument was calibrated using indium. The degree of crystallinity (X_c) was determined from the heat of fusion (ΔH_m) and the enthalpy of cold crystallization (ΔH_{cc}) using the following expression:

$$X_c = \frac{\Delta H_m + \Delta H_{cc}}{-126.6} \times 100, \qquad (1)$$

where -126.6 J g^{-1} is used as the heat of fusion of the crystalline phase of PET [18].

Infrared spectroscopy measurements were performed using a Fourier-transform infrared (FT-IR) spectrometer (FT/IR 4200, JASCO Co.) at a resolution of 4 cm^{-1}. Each spectrum was obtained from 80 scans.

Fig. 2 shows the apparatus used for CO_2-laser supersonic drawing. It consists of a spool to supply the fiber, a continuous-wave CO_2 laser with an output wavelength of 10.6 μm and a maximum power of 30 W, an acrylic vacuum chamber with Zn–Se windows and seven 0.5-mm-diameter fiber injection orifices for injecting the fibers, a power meter, a movable platen, and a vacuum pump. The acrylic vacuum chamber had a winding spool to collect nanofibers. The vacuum chamber was placed on the movable platen, which consists of a micro-alignment stage, a laboratory jack, and a turntable that can be moved parallel to the Y and Z axes and that can be rotated about the laser irradiation point on the fiber, allowing fine adjustments to be made.

Fig. 3(a) and (b) respectively shows photographs of a nanosheet wound onto the winding spool with a diameter of 6 cm and a length of 19 cm and of a rectangular nanosheet, which is about 17 cm wide and 18 cm long, that has been detached from the winding spool. Seven nanofibers were ultradrawn using the apparatus with seven orifices and were wound on the winding spool that rotated at a fixed speed, enabling a uniform nanosheet to be obtained.

The drag force exerted on the fiber in the air jet was estimated by performing fluid analysis using a three-dimensional (3D) finite element method (FEM) with ANSYS® CFZ 11.0 software.

3. Results and discussion

3.1. Collecting point dependence of fiber diameter

In this study, the apparatus with seven orifices was used for CLSMD. The seven orifices were aligned in a straight line at intervals of 10 mm. When performing CLSMD using this apparatus, it is very important to ensure that the fibers are uniformly irradiated by the laser beam in the air jet so that they produce a nanosheet composed of nanofibers with uniform diameters. To uniformly irradiate the fibers, it is necessary to ensure that the centers of the fibers accurately coincide with the center of the laser beam. This was done by aligning the vacuum chamber using the micro-alignment stage, the laboratory jack, and the turntable. To confirm that the seven fibers were uniformly drawn, the fiber diameters were measured at various points on nanosheets formed using different laser powers. Fig. 4 shows the average fiber diameter as a function of the longitudinal displacement (L) along the winding spool. The laser power was varied in the range 10–30 W. During these experiments, the fiber supply speed, chamber pressure, winding speed, and collecting time were kept constant at 0.1 m min^{-1}, 14 kPa, 75.4 m min^{-1}, and 5 min, respectively. The displacement of the beam side of the winding spool was set to $L = 0$.

At laser power of 10 W and 15 W, the fibers diameter increase greatly with displacement, from 590 nm and 489 nm at $L = 1$ cm to 1.26 μm and 647 nm at $L = 18$ cm, respectively. In contrast, the average fiber diameters at laser power of 20 W and 30 W were constant with L, being approximately 400 nm and 300 nm, respectively. At low laser powers, the fiber diameters vary greatly with L and thinner nanofibers were not obtained even when the center of fiber axis deviates slightly from the center of the laser beam because the laser power is too low to melt the fiber. On the other hand, the fiber diameter is considered to be independent of L at high laser powers because the laser power is still sufficiently high to melt the fiber even if the center of the laser deviates somewhat from the center of the fiber.

Laser irradiation must be performed at laser powers above 20 W to produce a nanosheet composed of uniform-diameter nanofibers. Henceforth, the laser irradiation performed in this study was conducted at a laser power of 20 W.

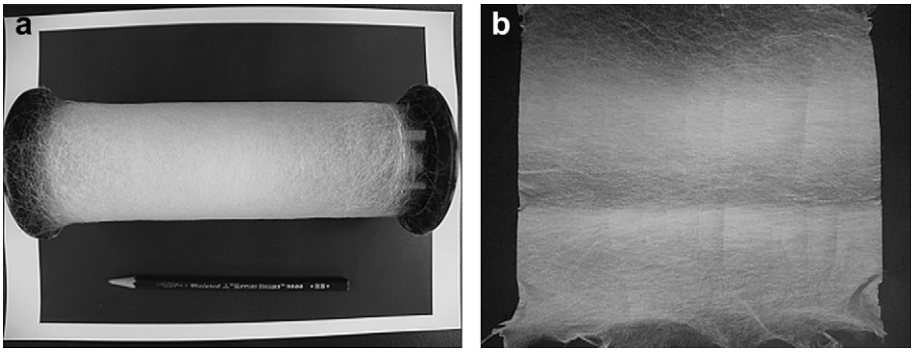

Fig. 3. Photographs of (a) a nanosheet wound onto the winding spool, which has a diameter of 6 cm and a length of 19 cm and of (b) a rectangular nanosheet about 17 cm wide and 18 cm long detached from the winding spool.

3.2. *Chamber pressure dependence of the nanosheet morphology*

Based on computer simulations described in our previous paper [16], the flow velocity was found to increase linearly with decreasing chamber pressure. The fiber is subjected to a drag force in the supersonic jet and is ultradrawn to a draw ratio of the order of 10^5.

To estimate the drag force acting on the fiber in the supersonic jet, the forces parallel and perpendicular to the fiber surface (the shear and compressive forces, respectively) were analyzed by 3D FEM.

Fig. 5(a) and (b) respectively shows the shear and compressive forces imparted to the fiber surface in the fiber-axis direction as functions of distance from the orifice, and Fig. 5(c) shows the 3D model used to simulate these forces. The shear and compressive forces are determined from their values at the nodes along the fiber axis (see Fig. 5(c)). After reaching a maximum value at a distance of 3.4 mm from the orifice, the shear force decreases rapidly with increasing distance from the orifice. The shear force increases as the chamber pressure decreases (i.e., as the flow velocity decreases). The compressive force is a maximum at the orifice outlet and decreases rapidly with distance from the orifice. The shear and compressive forces are both high at a distance of about 3 mm from the orifice. The drag force increases with decreasing chamber pressure (i.e., with increasing flow velocity).

The adiabatic expansion of air across the orifice cools the jet. Because the conservation of energy applies along streamlines, the following relation holds between the ratio of the temperature before adiabatic expansion (T_0) to the temperature after adiabatic expansion (T) and the Mach number (M) [19]:

$$\frac{T}{T_0} = \left\{ 1 + \frac{(\gamma - 1)M^2}{2} \right\}^{-1}, \tag{2}$$

where γ ($=C_p/C_v$) is the ratio of the heat capacity at constant pressure (C_p) to that at constant volume (C_v); in the case of air, γ is 1.4 because air consists principally of diatomic gases. The flow velocity is converted into a Mach number by dividing it by the sonic speed at a temperature of T_0:

$$M = \frac{v}{C} = \frac{v}{331.5 + 0.6(T_0 - 273.5)} \tag{3}$$

Fig. 6 shows relationship between the chamber pressure (i.e., the flow velocity) and the temperature (T) in the air jet, which was estimated using equation (2). The temperature (T) of the air jet decreases linearly with decreasing chamber pressure, and it is as low as 235 K at 6 kPa. The fiber is heated by laser beam irradiation in a low-temperature atmosphere.

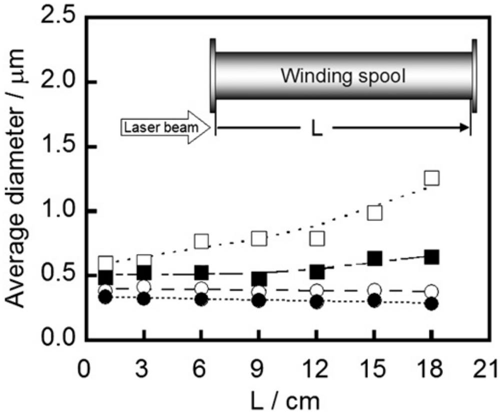

Fig. 4. Average diameter at four different laser powers (P_L) as a function of the displacement (L) in the longitudinal direction of the winding spool, □: $P_L = 10$ W; ■: $P_L = 15$ W; ○: $P_L = 20$ W; ●: $P_L = 30$ W.

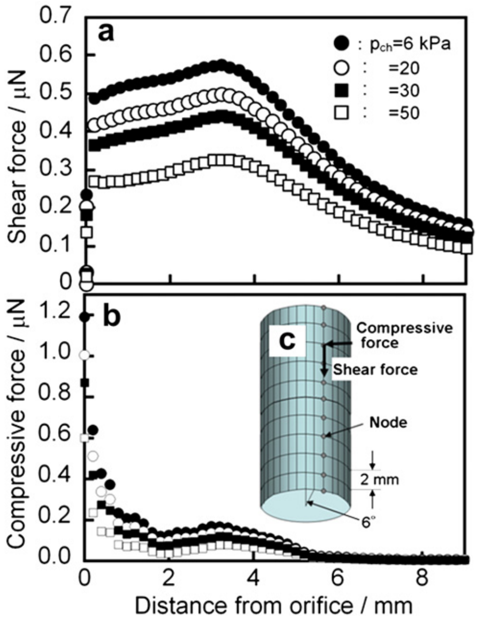

Fig. 5. Variations in the (a) shear and (b) compressive forces at the node of the fiber surface in the Z-axis direction with distance from the orifice, and (c) the 3D model used to simulate the shear and compressive forces.

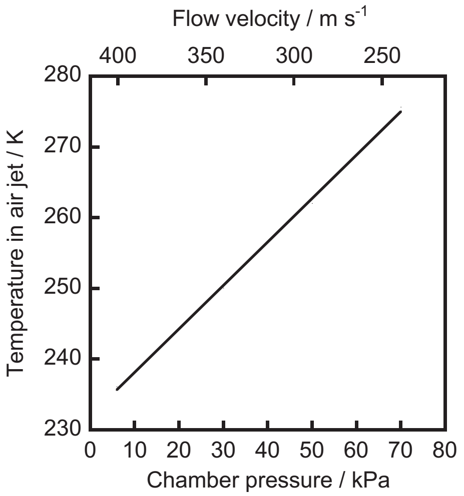

Fig. 6. Dependence of the average fiber diameter on the chamber pressure and the flow velocity.

In conventional fiber drawing, the drag force on the fiber acts only along the fiber axis, but in CLSMD the fiber is simultaneously subjected to forces both parallel and perpendicular to its surface. CLSMD is characterized by the compressive force applied perpendicular to the fiber surface. The resultant force of the shear and compressive forces is critical for supersonic drawing a molten fiber heated by a high-power laser beam without causing the molten fiber to expand.

Fig. 7 shows the dependence of the average fiber diameter on the chamber pressure. During this series of experiments, the fiber supply speed and the laser power were held constant at 0.-1 m min^{-1} and 20 W, respectively. The upper *X*-axis shows the flow velocity estimated by applying Graham's theorem:

$$v = \left\{\frac{2(p_0 - p)}{\rho}\right\}^{\frac{1}{2}} \tag{4}$$

where p_0 is atmospheric pressure, p is the vacuum chamber pressure, and ρ is the density of air (=1.2 g l^{-1}). The flow velocity estimated using equation (4) and the value obtained by 3D FEM almost agree, as mentioned in a previous paper [16]. The chamber pressure can be easily estimated using equation (4).

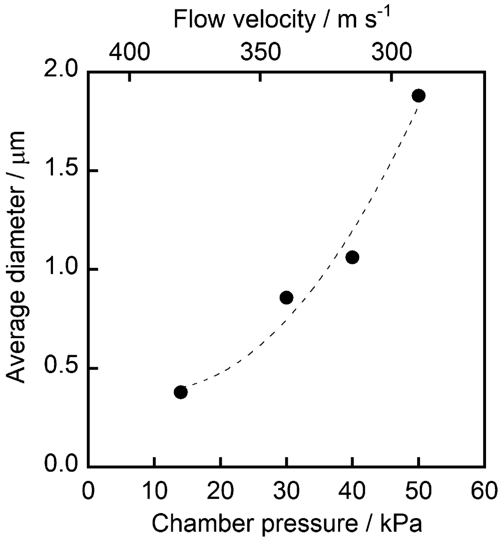

Fig. 7. Average fiber diameter as a function of the chamber pressure.

The average fiber diameter decreases significantly as the chamber pressure decreases; it is less than 1 µm at a chamber pressure of 30 kPa (i.e., a flow velocity of about 340 m s^{-1}). An increase in the flow velocity implies an increase in the drag force in the supersonic jet. A larger drag force induces a higher plastic flow rate, resulting in a thinner nanofiber being produced.

Fig. 8 shows histograms that indicate the diameter distribution and SEM micrographs at a magnification of 5000 for nanofibers produced at four different chamber pressures. The thinnest nanofibers with the narrowest diameter distribution were obtained at $p_{ch} = 14$ kPa. The SEM micrographs clearly show that the fiber diameter decreases as the chamber pressure is reduced. The SEM micrographs also reveal that the obtained nanofibers have smooth surfaces with no droplets.

To assess whether flow-induced orientation or flow-induced crystallization occurred during CSMD, FT-IR measurements were performed for nanosheets produced at various chamber pressures. Fig. 9 shows the change in the ratio of the intensity of the *trans* band at 848 cm^{-1} to that of the *gauche* band at 895 cm^{-1} with

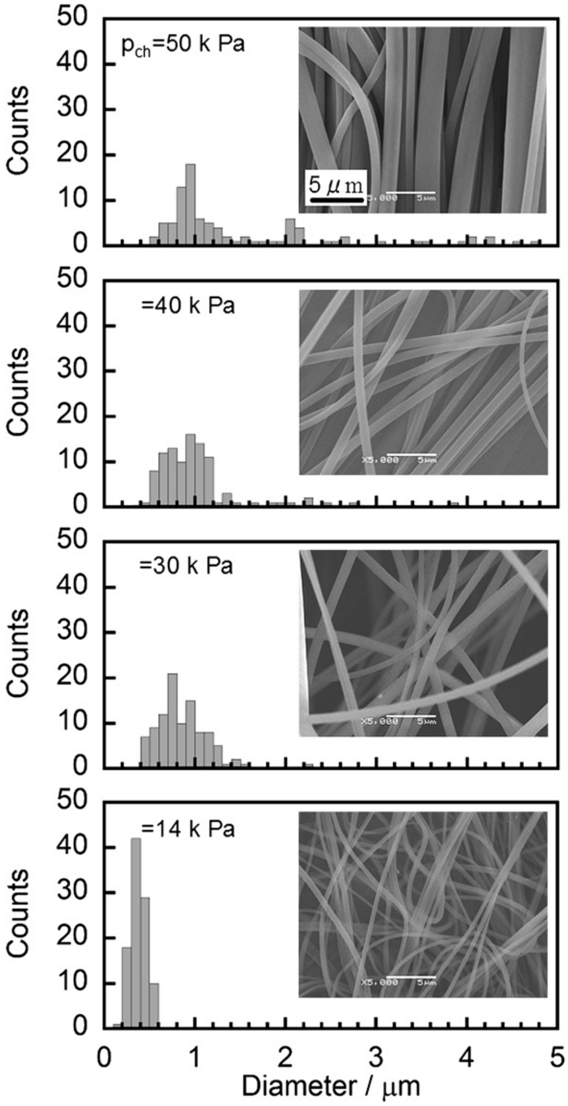

Fig. 8. Histograms showing the diameter distribution and SEM micrographs at a magnification of 5000 of nanofibers produced at four different chamber pressures.

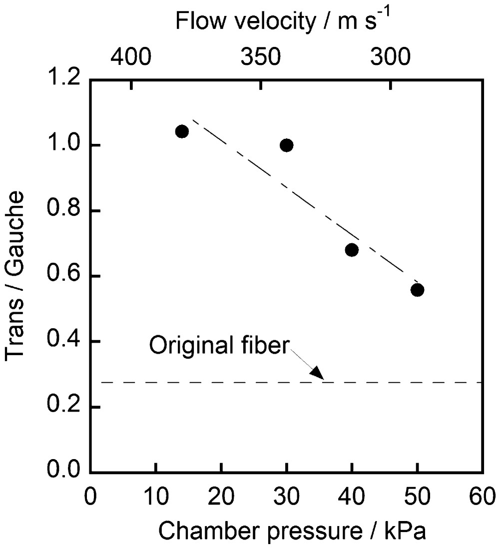

Fig. 9. Ratio of intensity of the *trans* band at 848 cm^{-1} to that of the *gauche* band at 895 cm^{-1} as a function of chamber pressure.

chamber pressure. The two bands have been assigned to CH_2 rocking of glycol [20–23].

The *trans* conformation can be present in both crystalline and amorphous phases [24], but the *gauche* conformation is found only in the amorphous phase [25]. The *trans*/*gauche* ratio of the original fiber was 0.273; the original fiber contains a high amount of the *gauche* conformation because it is an as-spun fiber. The *trans*/*gauche* ratio increases as the chamber pressure decreases. The increase in the amount of the *trans* conformation can be attributed to a morphological change from a folded chain to an extended chain. The polymer chain was further extended by flow-induced deformation in the faster supersonic jet. This conformational change implies that flow-induced orientation and flow-induced crystallization occur in the supersonic jet. The flow-induced orientation increases the extension, the orientation in the amorphous chain along the fiber axis, and the formation of crystal seeds. The flow-induced crystallization causes the crystallites to grow parallel to the fiber axis. A larger drag force is generated in the faster supersonic jet and it gives rise to flow-induced orientation and flow-induced crystallization.

Fig. 10 shows DSC curves for the original fiber and for nanosheets obtained at various chamber pressures. The original fiber exhibits a single exothermic peak at 127 °C due to cold crystallization and a broad melting endothermic peak at 255 °C. The melting peak can be ascribed to lamellar crystals, which form during DSC scanning. All the nanosheets have an exothermic peak at 117 °C due to cold crystallization and a shoulder on the low-temperature side of this peak; their peaks are 10 °C lower than that of the original fiber. This shift in T_{cc} to a lower temperature is caused by an increase in the degree of orientation of the amorphous chains and by crystal seeds formed during CSMD. The existence of a cold crystallization peak with a shoulder suggests that the amorphous chains have different degrees of orientation.

The nanosheets obtained at $p_{ch} = 40$ and 50 kPa have a melting peak at 255 °C and a shoulder on the high-temperature side of this peak, and their melting peaks are located at same temperature as that of the original fiber. The nanosheets produced at $p_{ch} = 14$ and 30 kPa have two melting peaks at 255 and 268 °C. The lower melting peak is observed at the same temperature as that of the original fiber, whereas the higher melting peak is 10 °C higher than the lower one. The higher melting peak is caused by an increase in the degree of perfection of the crystallites. Although we have reported the DSC behavior of PET drawn and annealed fibers [26], the high-temperature peak in Fig. 10 has never been observed previously. Crystallites with high melting temperatures exist only in nanosheets made of thinner nanofibers. The nanosheets produced at $p_{ch} = 14$ and 30 kPa exhibit the highest degrees of perfection of the crystallites.

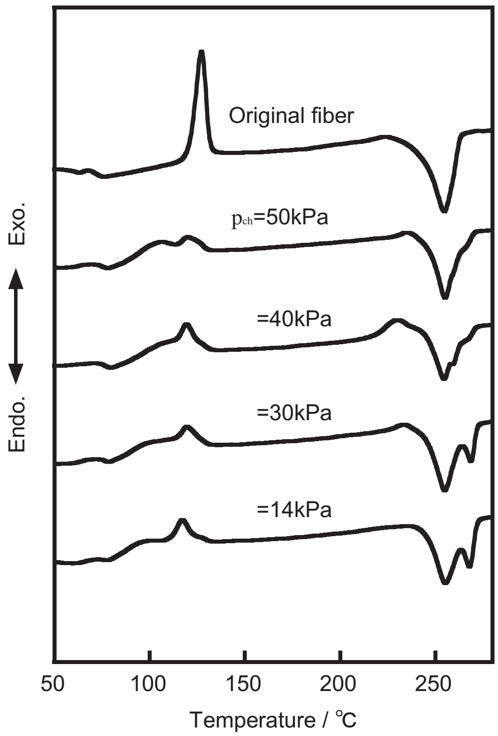

Fig. 10. DSC curves for the original fiber and nanosheets obtained at four different chamber pressures.

Table 1 lists the enthalpy of cold crystallization (ΔH_{cc}), the heat of fusion (ΔH_m), and the degree of crystallinity (X_c) estimated from ΔH_{cc} and ΔH_m for the original fiber and nanosheets produced at a supply speed of 0.1 m min^{-1}, a laser power of 20 W, and four different chamber pressures (p_{ch}). X_c of the original fiber is 19%, while those of the nanosheets produced at $p_{ch} = 40$ and 50 kPa are about 20%, and those of the nanosheets produced at $p_{ch} = 14$ and 30 kPa are about 30%. In a previous study [26], a PET fiber zone-drawn using a CO_2 laser was found to have $X_c = 33\%$; the nanosheets produced at $p_{ch} = 14$ and 30 kPa have similar values of X_c as the zone-drawn PET fiber. The DSC measurements clearly reveal that flow-induced crystallization during CSMD formed crystallites with a high degree of perfection. The crystallites formed in the supersonic jet oriented parallel to the fiber axis, as mentioned in a previous paper [15].

Table 1
Enthalpy of cold crystallization (ΔH_{cc}), heat of fusion (ΔH_m) and degree of crystallinity (X_c) of the original fiber and PET nanosheets produced at a supply speed of 0.1 m min^{-1}, a laser power of 20 W, and four different chamber pressures (p_{ch}).

Fiber	ΔH_{cc}/J g^{-1}	ΔH_m/J g^{-1}	X_c/%
Original	28.64	−52.48	19
$p_{ch} = 50$ kPa	10.96	−40.54	23
$p_{ch} = 40$ kPa	14.00	−40.80	21
$p_{ch} = 30$ kPa	10.77	−49.64	31
$p_{ch} = 14$ kPa	9.19	−49.22	32

3.3. Winding speed dependence of the nanosheet properties

Fig. 11 shows histograms of the fiber diameter distributions and SEM micrographs of nanosheets wound at four different winding speeds. The average fiber diameter and fiber diameter distribution are independent of the winding speed. The winding speed does not influence the fiber diameter and the superstructure because the fiber was ultradrawn in a supersonic jet so that the winding speed was much slower than the drawing speed.

The SEM micrographs reveal that the nanofibers are orientated in the winding direction only for the nanosheet wound at highest winding speed of 113 m min^{-1}. The winding speed affects the nanofiber arrangement, but it does not influence the fiber diameter or the superstructure.

Fig. 12 shows the winding speed dependence of the mechanical properties in the machine direction (MD) and the traverse direction (TD) for nanosheets wound at four different winding speeds. As the winding speed increases, Young's modulus and the tensile strength in the MD tend to increase, but those in the TD decrease slightly. The elongation in the MD decreases and that in the TD increases slightly with increasing winding speed. The mechanical anisotropy of Young's modulus and the tensile strength depend on the winding speed. Although the SEM micrographs did not reveal nanofiber orientation in the winding direction, the winding speed affects the degree of the arrangement of the nanofibers and their mechanical properties.

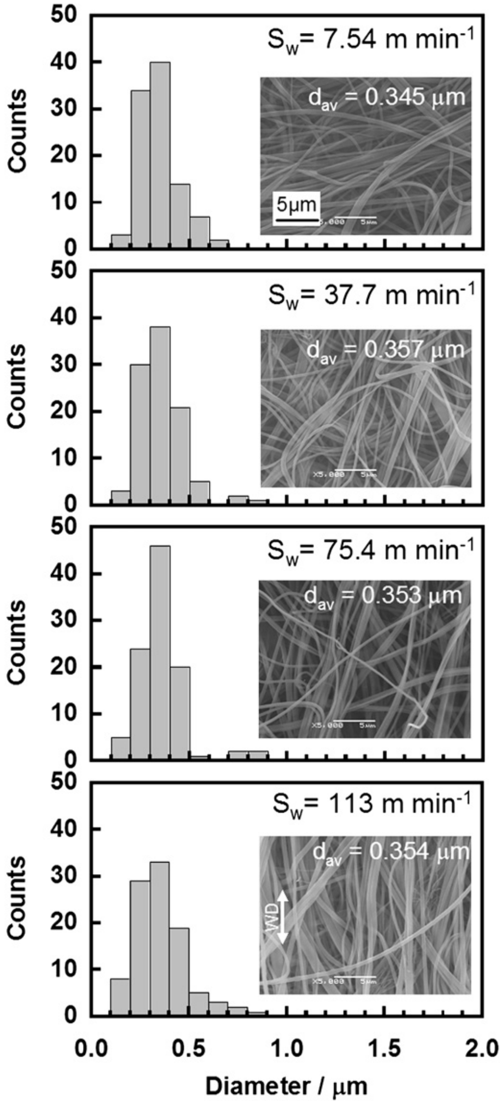

Fig. 11. Histograms showing fiber diameter distributions and SEM micrographs of nanosheets wound at four different winding speeds.

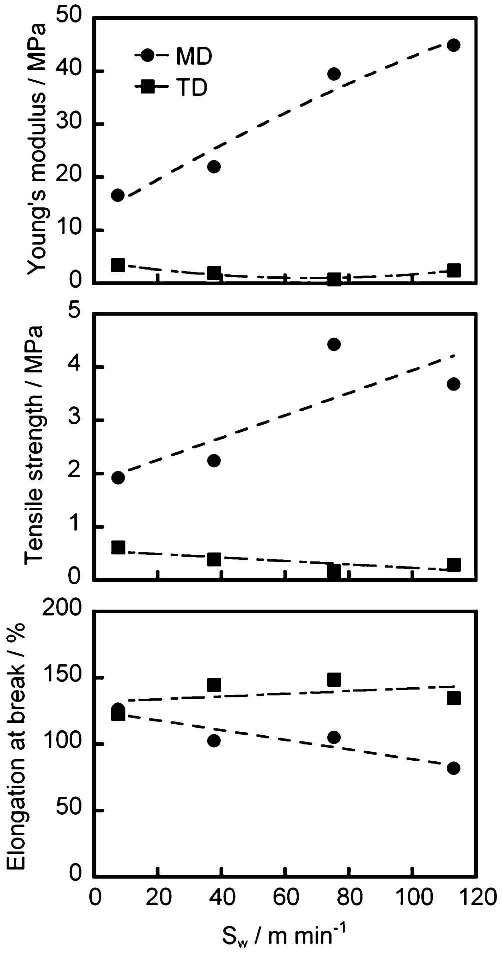

Fig. 12. Winding speed dependence of the mechanical properties in MD and TD for nanosheets wound at four different winding speeds.

4. Conclusion

PET nanosheets were obtained by winding nanofibers produced by CLSMD. In CLSMD, seven fibers can be simultaneously ultradrawn using only a single laser. The obtained nanofibers were wound on a winding spool. The obtained nanosheet was composed of uniform-diameter nanofibers. PET fibers were melted by laser irradiation and they experienced a drag force in the supersonic jet, which was cooled by adiabatic expansion at the fiber injection orifice. They were instantaneously ultradrawn to form nanofibers. The drag force induced not only morphological deformation but also conformational change in the molecular chain and crystallization. The extension of the molecular chain and the degree of the crystallinity both increased with decreasing chamber pressure (i.e., increasing drag force).

The winding speed used to collect the nanofibers influenced the anisotropy of the mechanical properties of the nanosheets, but it did not affect the fiber diameter or the superstructure.

CLSMD can be used for all thermoplastic polymers without using a solvent and without the need to remove a second component. It can be used to produce nanofibers of indefinite length because the fiber is supplied at a constant speed and is continuously irradiated by the laser beam. CLSMD can be used to easily prepare various nanosheets using CO_2-laser irradiation and it does not require any additional processes. CLSMD is a novel method for producing nanosheets using only a CO_2 laser.

Acknowledgment

The authors acknowledge financial support from a Grant-in-Aid for Scientific Research (B) from the Japan Society for the Promotion of Science.

References

[1] Ding B, Kimura E, Sato T, Fujita S, Shiratori S. Polymer 2004;45:1895–902.
[2] Gupta P, Wilkes GL. Polymer 2003;44:6353–9.
[3] Ayutsede J, Gandhi M, Sukigara S, Micklus M, Chen HE, Ko F. Polymer 2005;46:1625–34.
[4] Fong H. Polymer 2004;45:2427–32.
[5] Kim JS, Reneker DH. Polym Eng Sci 1999;38:849–54.
[6] Deitzel JM, Kleinmeyer J, Harris D, Tan BNC. Polymer 2001;42:261–72.
[7] Huang C, Chen S, Reneker DH, Lai C, Hou H. Adv Mater 2006;18:668–71.
[8] Pedicini A, Farris RJ. Polymer 2003;44:6857–62.
[9] Varabhas JS, Chase GG, Reneker DH. Polymer 2008;49:4226–9.
[10] Zhou H, Green TB, Joo Y. Polymer 2006;47:7497–505.
[11] Dalton PD, Grafahrend D, Klinkhammer K, Klee D, Möller M. Polymer 2007;48:6823–33.
[12] Lyons J, Li C, Ko F. Polymer 2004;45:7597–603.
[13] Ellison CJ, Phatak A, Giles DW, Macosko CW, Bates FS. Polymer 2007;48:3306–16.
[14] Borkar S, Gu B, Dirmyer M, Delicado R, Sen AN, Jackson BR, et al. Polymer 2006;47:8337–43.
[15] Suzuki A, Aoki K. Eur Polym J 2008;44:2499–505.
[16] Suzuki A, Tanizawa K. Poymer 2009;50:913–21.
[17] Suzuki A, Yamada Y. J Appl Polym Sci; in press.
[18] Brandrup J, Immergut EH, editors. Polymer handbook. 4th ed. New York: J. Wiley & Sons; 1998. p. VI/42.
[19] Hagena OF. Surf Sci 1981;106:101–16.
[20] Quintanilla L, Rodrı́guez-Cabello JC, Jawhari T, Pastor JM. Polymer 1993;34:3787–95.
[21] Lin SB, Koenig JL. J Polym Sci Polym Phys Ed 1982;20:2277–95.
[22] Yazdanian M, Ward IM, Brody H. Polymer 1985;26:1779–90.
[23] Andanson JM, Kazarian SG. Macromol Symp 2008;265:195–204.
[24] Pearce R, Cole KC, Ajji A, Dumolin MM. Polym Eng Sci; 1997:1795–800.
[25] Ajji A, Cole KC, Dumolin MM, Ward IM. Polym Eng Sci; 1997:1801–8.
[26] Suzuki A, Mizuochi D. J Appl Polym Sci; 2001:2775–83.